Forward simulation and inverse dipole localization with lowest order Raviart-Thomas elements for electroencephalography

S Pursiainen†, A Sorrentino‡, C Campi‡ and M Piana‡

†Aalto University, Mathematics, P.O. Box 11100, FI-00076 Aalto, Finland
‡Dipartimento di Matematica, Università di Genova, via Dodecaneso 35, I-16146 Genova, Italy

Abstract. Electroencephalography (EEG) is a non-invasive imaging modality in which a primary current density generated by the neural activity in the brain is to be reconstructed based on external electric potential measurements. This paper focuses on the finite element method (FEM) from both forward and inverse aspects. The goal is to establish a clear correspondence between the lowest order Raviart-Thomas basis functions and dipole sources as well as to show that the adopted FEM approach is computationally effective. Each basis function is associated with a dipole moment and a location. Four candidate locations are tested. Numerical experiments cover two different spherical multilayer head models, four mesh resolutions and two different forward simulation approaches, one based on FEM and one based on the boundary element method (BEM) with standard dipoles as sources. The forward simulation accuracy is examined through column- and matrix-wise relative errors as well as through performance in inverse dipole localization. A closed-form approximation of dipole potential was used as the reference forward simulation. The results suggest that the present approach is comparable or superior to BEM and to the recent FEM based subtraction approach regarding both accuracy, computation time and accessibility of implementation.

PACS numbers: 87.19.le, 87.10.Kn, 02.30.Zz

AMS classification scheme numbers: 35Q60, 65M60, 15A29

1. Introduction

Electroencephalography (EEG) [22] is an non-invasive imaging modality in which a primary current density generated by the neural activity in the brain is to be reconstructed based on external electric potential measurements. Recovery of the neural current is an ill-posed inverse problem [15, 25] which can be approached through regularization methods [12, 19, 24, 25, 28, 33, 31] that deal with the intrinsic characteristics of the problem and with the very low signal-to-noise ratio of the input data. As for all the inverse problems, the availability of forward methods [18, 20, 30, 8, 34] allows the creation of synthetic data, enabling the validation of the

inverse source methods. In the case of EEG, forward methods play a crucial role, because the dependence of the measurements on the neural current is only implicit as a consequence of the complex conductivity structure of the brain.

This paper focuses on the finite element method (FEM) from both forward and inverse aspects [21, 26]. The advantage of FEM is that it allows accurate modeling of the conductivity distribution inside the head. This is important, since the highly anisotropic conductivities of the skull and the brain have a strong effect on the electromagnetic field outside the head [17, 32]. Modeling the effect of complex anisotropic conductivities is infeasible through the standard Boundary Element Method (BEM) [3], which is presently one of the predominant EEG forward simulation methods in practical applications [22, 2, 9, 16].

The present FEM approach relies on both nodal and Raviart-Thomas elements [5, 21]. In particular, the goal is to show how and to what extent the lowest order Raviart-Thomas basis functions can model the dipole sources in computationally effective fashion. These basis functions are, in general, the simplest ones that have a square integrable divergence, which is necessary, when FEM is used for computing the potential field [5, 21]. Further, in contrast to the standard dipoles, which have a single-point support, finite element basis functions are finitely supported. Even though the real neural currents are not dipoles, practical applications of EEG are often based on the assumption of dipole sources, which makes it important to study how well the present source model corresponds to the standard one. This work associates each lowest order Raviart-Thomas basis function with a dipole moment and a location. Four *ad hoc* candidate locations are introduced and tested numerically. The primary reason for studying these different candidates is that the Raviart-Thomas element degrees of freedom are by definition not nodal but facial [5]. And the secondary motivation is to obtain knowledge on how strongly the forward simulation accuracy depends on the source location.

The numerical experiments cover two different spherical multilayer head models, four different mesh resolution levels as well as two different forward simulation approaches, one based on FEM and one based on BEM with standard dipoles as sources. The performance of the forward simulations is examined through relative errors and accuracy in inverse dipole localization [15]. The data used as a reference is computed using a closed-form approximation of the analytical solution. The results obtained suggest that the present FEM approach is comparable or even superior to the BEM and also to the recent and effective FEM based subtraction approach [18, 8] regarding both accuracy and computation time. Additionally, implementation of the present approach was found to be accessible due to the sufficiency of low-order numerical integration methods (quadratures) [5].

This paper is organized as follows. Section 2 describes the forward methods applied in this study including the EEG forward model and simulation, the present source model as well as the other applied finite element techniques. Section 3 reports the numerical experiments with EEG. Finally, section 4 summarizes the results and suggests possible

directions for the future work.

2. Forward methods

2.1. Forward model

The EEG forward model associates a given primary current density $\mathbf{J}^p$ in the head Ω with a measurement data vector $\mathbf{y}$ containing electric potential values. The data are obtained using electrodes. The electric potential field u in Ω is of the form $\mathbf{E} = -\nabla u$ and the total current density is given by $\mathbf{J} = \mathbf{J}^p + \mathbf{J}^s = \mathbf{J}^p - \sigma\nabla u$, in which σ is the conductivity distribution of Ω and $\mathbf{J}^s = -\sigma\nabla u$ is called the secondary or the volume current density. Replacing the total current density into the charge conservation law $\nabla \cdot \mathbf{J} = 0$ and assuming that the current flow out of Ω is zero results into the second order partial differential equation $\nabla \cdot (\sigma\nabla u) = \nabla \cdot \mathbf{J}^p$ in Ω with the Neumann boundary condition $\partial u/\partial \mathbf{n} = 0$ on the boundary $\partial\Omega$. These again yield the weak form [5, 21]

$$\int_\Omega \sigma\nabla u \cdot \nabla v \,\mathrm{d}V = -\int_\Omega (\nabla \cdot \mathbf{J}^p) v \,\mathrm{d}V, \quad \text{for all } v \in H^1(\Omega), \tag{1}$$

which has a unique solution $u \in H^1(\Omega) = \{w \in L^2(\Omega) : \partial w/\partial x_i \in L^2(\Omega),\, i = 1, 2, 3\}$, if the potential zero reference level is given, and if the divergence of the primary current density is square integrable, meaning that $\mathbf{J}^p \in \mathbf{H}(\mathrm{div};\, \Omega) = \{\, \mathbf{w} \in (L^2(\Omega))^3 : \nabla \cdot \mathbf{w} \in L^2(\Omega)\}$. The weak form (1) constitutes the present EEG forward model, i.e. the dependence of u on $\mathbf{J}^p$, which is linear and defined for all $\mathbf{J}^p \in \mathbf{H}(\mathrm{div};\, \Omega)$.

2.2. Forward simulation

In the numerical simulation of the forward model, the unknown of the inverse problem is identified with a finite dimensional vector $\mathbf{x}$ that is linked with a noiseless data vector $\mathbf{y}$ as given by

$$\mathbf{y} = \mathbf{L}\mathbf{x}, \tag{2}$$

in which $\mathbf{L}$ is known as the lead field or the transfer matrix. The discretized versions of the potential u and of the current density $\mathbf{J}^p$ are defined as $u_{\mathcal{T}} = \sum_{i=1}^N z_i \psi_i$ and $\mathbf{J}^p_{\mathcal{T}} = \sum_{k=1}^M x_k \,\mathbf{w}_k$, where $\psi_1, \psi_2, \ldots, \psi_N \in H^1(\Omega)$ and $\mathbf{w}_1, \mathbf{w}_2, \ldots, \mathbf{w}_M \in H(\mathrm{div};\Omega)$ are finite element basis functions corresponding to a shape regular finite element mesh $\mathcal{T}$. Furthermore, it is assumed that the electrodes coincide with the vertices $i_1, i_2, \ldots, i_L$ of the finite element mesh.

The coefficients $z_1, z_2, \ldots, z_N$ and $x_1, x_2, \ldots, x_M$ define unknown coordinate vectors $\mathbf{z}$ and $\mathbf{x}$, which satisfy the linear system $\mathbf{A}\mathbf{z} = \mathbf{G}\mathbf{x}$, resulting from the Ritz-Galerkin discretization [5] of the weak form (1). The entries of $\mathbf{A}$ and $\mathbf{G}$ are given by

$$a_{ij} = \int_\Omega \sigma\nabla\psi_i \cdot \nabla\psi_j \,\mathrm{d}V \quad \text{and} \quad g_{ik} = -\int_\Omega (\nabla \cdot \mathbf{w}_k)\psi_i \,\mathrm{d}V. \tag{3}$$

Additionally, to establish the positive definiteness and thereby the invertibility of the symmetric matrix $\mathbf{A}$, all the entries on the i_1th row and column of $\mathbf{A}$ are set to

zero except $a_{i_1,i_1} = 1$. Following from the equation $\mathbf{Az} = \mathbf{Gx}$, the EEG potential measurements with the eventual potential zero reference level, that is the mean value of the electrode potentials, can be obtained choosing the lead field matrix as

$$\mathbf{L} = \mathbf{RA}^{-1}\mathbf{G}, \tag{4}$$

in which $\mathbf{R}$ is a $L \times N$ restriction matrix with $r_{i_\ell i_{\ell+1}} = 1 - \frac{1}{L}$, $r_{i_\ell i_k} = -\frac{1}{L}$, if $\ell \neq k+1$, $\ell \leq L$ and $k \leq L$, and all the other entries are zero. Since the number of rows of $\mathbf{L}$ is usually much lower than the number of columns, it is advantageous [11] to compute $\mathbf{RA}^{-1}$ row by row, through e.g. an iterative solver, without forming the inverse $\mathbf{A}^{-1}$.

Table 1. The applied spherical multilayer head models, radiuses of the layers as well as radial and tangential conductivities in different layers.

		Layers			
Model	Quantity	Brain	CSF[a]	Skull	Scalp
(I)	Layer radius	0.87	-	0.92	1.00
	Radial conductivity	0.33	-	0.0042	0.33
	Tangential conductivity	0.33	-	0.0042	0.33
(II)	Layer radius	0.78	0.80	0.86	0.92
	Radial conductivity	0.33	1.79	0.0042	0.33
	Tangential conductivity	0.33	1.79	0.042	0.33

[a] Cerebrospinal fluid.

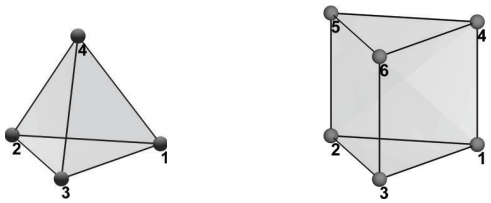

Figure 1. A tetrahedral element on the left and a prismatic element on the right.

2.3. Spherical multi-layer head models

As the domain Ω, this work uses spherical multi-layer head models which consist of layers (compartments) formed by concentric spheres. The innermost layer is spherical and represents the brain. In each layer, the conductivity distribution σ is constant in magnitude. The model is called anisotropic, if the conductivity is anisotropic in at least one of the layers, and otherwise it is called isotropic.

The models used are an isotropic three-layer [34, 1] and an anisotropic four-layer model [18, 8, 29] denoted by (I) and (II), respectively. The isotropic one is the Ary

model consisting of a brain, a skull, and a scalp layer. The anisotropic one is similar to the Stok model including a cerebrospinal fluid (CSF) layer between the brain and the skull. The only anisotropic layer in (II) is the skull in which the tangential conductivity compared to the radial one is ten times larger. The radiuses as well as the radial and tangential conductivities of the different layers of (I) and (II) have been reported in table 1.

2.4. Finite element mesh

The multilayer structure of Ω is incorporated into the finite element mesh. This work uses meshes in which the brain layer consists of tetrahedral elements and the thin surface layers of prisms [26], which provide an efficient way to control the element size in the radial direction. Both applied element types are illustrated in figure 1. The electric potential is supported on both the tetrahedral and the prismatic part of the mesh. The source currents are assumed to exist only in the tetrahedral part, i.e. in the brain layer.

2.5. Nodal basis functions

The potential distribution is discretized using nodal (Lagrangian) basis functions [5, 26] for both the tetrahedral and the prism elements. The nodal basis function ψ_i obtains the value one in the i:th vertex of the finite element mesh and vanishes in all the other vertices. As a result, the value of the $u_{\mathcal{T}}$ at the i:th vertex coincides with the i:th degree of freedom z_i of $u_{\mathcal{T}}$. The basis function restricted to one element can be obtained requiring that its value equals one in precisely one of the element vertices. In the tetrahedral case, the resulting polynomial is linear, and in the prism case, it is of second order, but linear on both the parallel triangular faces of the element and also in the normal direction of those faces. The nodal basis functions are piecewise continuous and form a subspace of $H^1(\Omega)$. The support of ψ_i, i.e. the set on which ψ_i differs from zero, is formed by the union of all the elements that include the ith vertex.

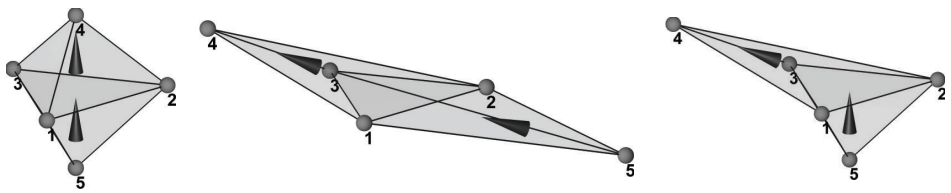

Figure 2. Three visualizations of a lowest order Raviart-Thomas basis function supported on two tetrahedral elements.

2.6. Lowest order Raviart-Thomas basis functions

The lowest order Raviart-Thomas [5, 21] basis function $\mathbf{w}_k$ is supported on two adjacent tetrahedral elements that share the kth face of the finite element mesh (figure 2). When

restricted to one of the supporting tetrahedrons, the basis function is the position vector field transferred and scaled, i.e. of the form

$$\mathbf{g}(\mathbf{r}) = c(\mathbf{r} - \hat{\mathbf{r}}), \tag{5}$$

where c is a scaling constant and $\hat{\mathbf{r}}$ denotes the position of the vertex opposite to the kth face. The divergence and the curl of $\mathbf{g}$ are given by $\nabla\cdot\mathbf{g} = 3c$ and $\nabla\times\mathbf{g} = 0$, respectively. The normal component of $\mathbf{w}_k$ vanishes on all the tetrahedron faces except the kth one, on which it is continuous. The scaling of $\mathbf{w}_k$ in each tetrahedron is chosen so that the norm of the normal component over the k:th face is one and thus continuous. As a result, the divergence of $\mathbf{w}_k$ is square integrable, i.e. $\mathbf{w}_k \in \mathbf{H}(\mathrm{div};\,\Omega)$. Additionally, this means that the k:th degree of freedom x_k of $\mathbf{J}^p_{\mathcal{T}}$ coincides with the normal component of $\mathbf{J}^p_{\mathcal{T}}$ on the k:th face.

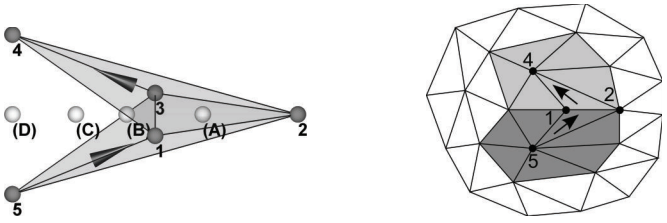

Figure 3. On the left: The candidate locations (A), (B), (C), and (D) corresponding to the illustrated lowest order Raviart-Thomas basis function. On the right: A two-dimensional visualization of a lowest order Raviart-Thomas source (arrows) and of the supports of the two nodal basis functions (two shades of grey) corresponding to the vertices 4 and 5 that communicate the effect of the source to the nodal basis.

2.7. Dipole model based on the lowest order Raviart-Thomas basis functions

When used as a source current for an electric field, a single basis function $\mathbf{w}_k$ is dipole-like, meaning that the electromagnetic field far enough from the source is similar to that of a dipole. A mathematical dipole is supported only at one point and identified by the pair $(\mathbf{q}, \mathbf{r})$, in which $\mathbf{q}$ is the dipole moment indicating the direction and strength and $\mathbf{r}$ is the location. To enable comparison of $\mathbf{w}_k$ to a dipole, $\mathbf{w}_k$ is given a dipole moment $\mathbf{q}_k$ and a location $\mathbf{r}_k$. The vector $\mathbf{q}_k$ is defined as the integral

$$\mathbf{q}_k = \int_\Omega \mathbf{w}_k \,\mathrm{d}x\mathrm{d}y\mathrm{d}z \tag{6}$$

and the location is formed as a weighted average $\mathbf{r}_k = (\sum_{\ell=1}^5 \alpha_\ell \mathbf{r}_k^{(\ell)})(\sum_{\ell=1}^5 \alpha_\ell)^{-1}$ of the vertex position vectors $\mathbf{r}_k^{(1)}, \mathbf{r}_k^{(2)}, \ldots, \mathbf{r}_k^{(5)}$ indexed according to figure 3. Four candidate locations (A), (B), (C), and (D), defined in table 2, are tested. The primary motivation for studying these *ad hoc* candidates is that the Raviart-Thomas element degrees of freedom are by definition not nodal but facial [5]; There is no single point that would *a priori* be the natural choice. And the secondary motivation is to obtain knowledge on how strongly the forward simulation accuracy depends on the source location.

Table 2. The candidates (A), (B), (C), and (D) tested as the source location.

Location	α_1	α_2	α_3	α_4	α_5
(A)	1/3	1/3	1/3	0	0
(B)	1/5	1/5	1/5	1/5	1/5
(C)	1/9	1/9	1/9	1/3	1/3
(D)	0	0	0	1/2	1/2

Location (A) is the centroid of the face associated with the degree of freedom. (D) is the center of the line segment between $\mathbf{r}_k^{(4)}$ and $\mathbf{r}_k^{(5)}$ and interesting, since the effect of each vector valued source function $\mathbf{w}_k$ on the potential field is communicated through the scalar valued nodal basis functions corresponding to $\mathbf{r}_k^{(4)}$ and $\mathbf{r}_k^{(5)}$ (see Appendix). Location (B) coincides with the center of mass of the convex hull defined by the vectors $\mathbf{r}_k^{(1)}, \mathbf{r}_k^{(2)}, \ldots, \mathbf{r}_k^{(5)}$. Both (B) and (C) lie on the line segment between (A) and (D). And the weight given to $\mathbf{r}_k^{(4)}$ and $\mathbf{r}_k^{(5)}$ increases from (A) to (D).

2.8. Boundary element method (BEM)

BEM [3] is currently one of the most popular methods in EEG forward simulation [22, 2, 9, 16]. It relies on surface meshes and elements instead of volume ones. One of the great advantages of BEM is that it allows the use of truly pointlike dipoles as the source currents. In contrast to FEM, modeling the effect of strongly inhomogenous or anisotropic conductivity distributions with BEM can be difficult or impossible.

In BEM, the boundary of the domain Ω as well as each interface between two different conductivity values needs to be discretized. The head models (I) and (II) can be discretized generating a surface mesh on the outer boundary of each layer. In this work, BEM meshes consist of triangular finite element mesh surfaces. The applied surface elements are linear, and the BEM forward simulation is provided by the MNE software package [14] for EEG/MEG computations.

2.9. Closed-form approximation of the analytical solution

When a spherical multi-layer head model is used, the analytical potential of a dipole $(\mathbf{q}, \mathbf{r})$ on the electrodes can be approximated in a closed form through the formula

$$u_j(\mathbf{q}, \mathbf{r}) \approx \sum_{\ell=1}^{K} u_j^{(s)}(\lambda_\ell \mathbf{q}, \mu_\ell \mathbf{r}), \tag{7}$$

in which $u_j(\mathbf{q}, \mathbf{r})$ is the potential of the jth electrode and $u_j^{(s)}(\mathbf{q}, \mathbf{r})$ is the corresponding single-layer sphere potential that has a relatively simple closed-form expression presented e.g. in [34]. The approximation (7) can be shown to converge rapidly towards the exact analytical solution as the number of terms K grows [34]. The multipliers $\lambda_1, \lambda_2, \ldots, \lambda_K$ and $\mu_1, \mu_2, \ldots, \mu_K$ are so-called Berg parameters [4] that can be computed through a

numerical optimization procedure. This work uses (7) to construct the reference forward simulation for the numerical experiments.

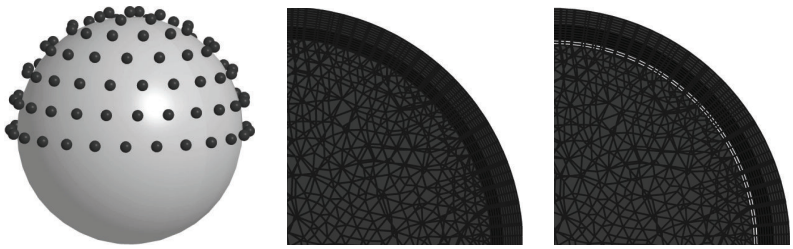

Figure 4. Visualization of the 102 measurement point locations (left) and the cross-section of the finite element mesh corresponding to head model (I) (center) and (II) (right). Both meshes were generated by first constructing the brain layer using tetrahedral elements and after that adding the relatively thin prismatic layers to cover the brain. The color shows the relative value of the radial conductivity in each visualized tetrahedron.

Table 3. The finite element meshes and the corresponding function bases as numbers: mesh and resolution level number and the number of elements, tetrahedra, prisms, outer faces, as well as of nodal and Raviart-Thomas basis functions.

Model	Resolution	Elements	Prisms	Boundary faces[a]	Nodal[b]	R-T[c]
(I)	1	221221	84357	136864	85287	163450
(I)	2	155904	59392	96512	60131	115072
(I)	3	127360	62464	64896	44191	122432
(I)	4	31552	7424	24128	13839	13920
(II)	1	231749	84357	147392	90553	163450
(II)	2	163328	59392	103936	63845	115072
(II)	3	132352	62464	69888	46689	122432
(II)	4	33408	7424	25984	14769	13920

[a] The number of faces on the outer boundary of the mesh.
[b] The number of nodal basis functions which coincides with the number of nodes.
[c] The number of Raviart-Thomas basis functions.

3. Numerical experiments

In the numerical experiments, the performance of the present FEM approach (4) with the lowest order Raviart-Thomas basis functions as dipole sources was tested within the head models (I) and (II). Additionally, the BEM solver of the MNE software package was tested in the case of the isotropic model (I). The closed-form approach (7) was used as the reference forward simulation method. The number of terms K in (7) was chosen to

Table 4. The Berg parameters $\mu_1, \mu_2, \ldots, \mu_{10}$ and $\lambda_1, \lambda_2, \ldots, \lambda_{10}$ used in the computation of the numerical closed-form approximation of the analytic solution.

	Model (I)		Model (II)	
ℓ	Berg λ_ℓ	Berg μ_ℓ	Berg λ_ℓ	Berg μ_ℓ
1	0.51346275	0.10663283	0.11989703	0.60731855
2	−0.45889827	0.098806681	0.18083646	0.44203404
3	0.062551069	0.32614976	0.0077327407	0.75566590
4	0.22554434	0.21740585	0.080699975	0.25268809
5	0.10838624	0.28368475	−0.018145067	0.0028600870
6	−0.31251690	0.19849838	0.079971766	0.74589779
7	0.23561751	0.52983366	−0.036228989	0.076998525
8	0.079372931	0.87488245	0.032252683	0.027354754
9	0.049310282	0.99979295	0.035003541	0.24186295
10	0.15808930	0.72895122	0.051230976	0.84980359

Table 5. The implemented FEM and BEM forward simulation tests.

					Computation time	
Test	Model	Method	Mesh resolution	Dipole location	32-bit (s)	64-bit (s)
(i)	(I)	FEM	1	(A)–(D)	822	353
(ii)	(I)	FEM	2	(A)–(D)	547	234
(iii)	(I)	FEM	3	(A)–(D)	382	164
(iv)	(I)	FEM	4	(A)–(D)	87	40
(v)	(II)	FEM	1	(A)–(D)	912	385
(vi)	(II)	FEM	2	(A)–(D)	583	264
(vii)	(II)	FEM	3	(A)–(D)	403	174
(viii)	(II)	FEM	4	(A)–(D)	97	43
(ix)	(I)	BEM	1 (surface)	Authentic	5400	-
(x)	(I)	BEM	2 (surface)	Authentic	1800	-
(xi)	(I)	BEM	3 (surface)	Authentic	600	-
(xii)	(I)	BEM	4 (surface)	Authentic	120	-

be 10. The Berg parameters $\mu_1, \mu_2, \ldots, \mu_{10}$ and $\lambda_1, \lambda_2, \ldots, \lambda_{10}$ (table 4) were computed as explained in [34] and the resulting relative error variances [34] were $5.15 \cdot 10^{-14}$ and $7.48 \cdot 10^{-15}$ for the head models (I) and (II), respectively.

The number of mesh resolutions tested was four. On each resolution level, the same tetrahedron structure was used for both models (I) and (II) (figure 4). The prism size in each layer was constant in the radial direction and independent of the resolution level. The number of the prismatic layers was chosen so that the relative prism size for (I) and (II) was similar and that the thinnest layer (CSF) contained more than one prism

Table 6. The relative error RE_L in the forward simulation tests (i)–(viii) with the dipole locations (A)–(D).

	Dipole location			
Test	(A)	(B)	(C)	(D)
(i)	0.0250	0.0158	0.0109	0.00948
(ii)	0.0416	0.0282	0.0216	0.0204
(iii)	0.0353	0.0251	0.0200	0.0181
(iv)	0.0791	0.0546	0.0451	0.0503
(v)	0.0163	0.00987	0.00594	0.00372
(vi)	0.0265	0.0167	0.0108	0.00715
(vii)	0.0225	0.0149	0.0105	0.00796
(viii)	0.0551	0.0359	0.0253	0.0213

Table 7. The maximum of dipole localization error LE_k and the percentage of the correctly localized dipoles for which $\mathrm{LE}_k = \mathrm{AE}_k = 0$.

	Dipole location							
	(A)		(B)		(C)		(D)	
Test	LE_k max.[a]	Zeros[b] (%)	LE_k max.[a]	Zeros[b] (%)	LE_k max.[a]	Zeros[b] (%)	LE_k max.[a]	Zeros[b] (%)
(i)	0.0527	69.116	0.0461	69.102	0.0256	69.136	0	100
(ii)	0.138	57.167	0.114	59.146	0.0596	59.365	0.0553	99.991
(iii)	0.135	56.946	0.115	58.709	0.0934	58.911	0.0735	99.981
(iv)	0.249	65.208	0.179	67.730	0.100	67.989	0.118	99.986
(v)	0.0527	69.300	0.0461	69.290	0.0256	69.378	0	100
(vi)	0.120	57.861	0.0956	59.315	0.0248	59.413	0	100
(vii)	0.121	57.272	0.103	58.660	0.0870	58.893	0.0659	99.997
(viii)	0.223	65.108	0.160	67.392	0.0481	67.486	0	100

[a] Maximum of the localization error LE_k, $i = 1, 2, \ldots, M$.
[b] Percentage of zeros of LE_k, $i = 1, 2, \ldots, M$.

layer to avoid forward simulation errors due to the discontinuity of the conductivity in the radial direction [5].

In each computed lead field matrix $\mathbf{L} = (\mathbf{l}_1, \mathbf{l}_2, \ldots, \mathbf{l}_M)$, the columns were normalized so that $\mathbf{l}_k$ corresponded to the data of the dipole source $(\mathbf{q}_k, \mathbf{r}_k)$ with $\|\mathbf{q}_k\|_2 = 1$ for $k = 1, 2, \ldots, M$. The number of rows and columns in the lead field matrix coincided with the number of the measurement points and of the dipole sources, respectively. The former one was 102 in each test (figure 4). The latter one was determined by the

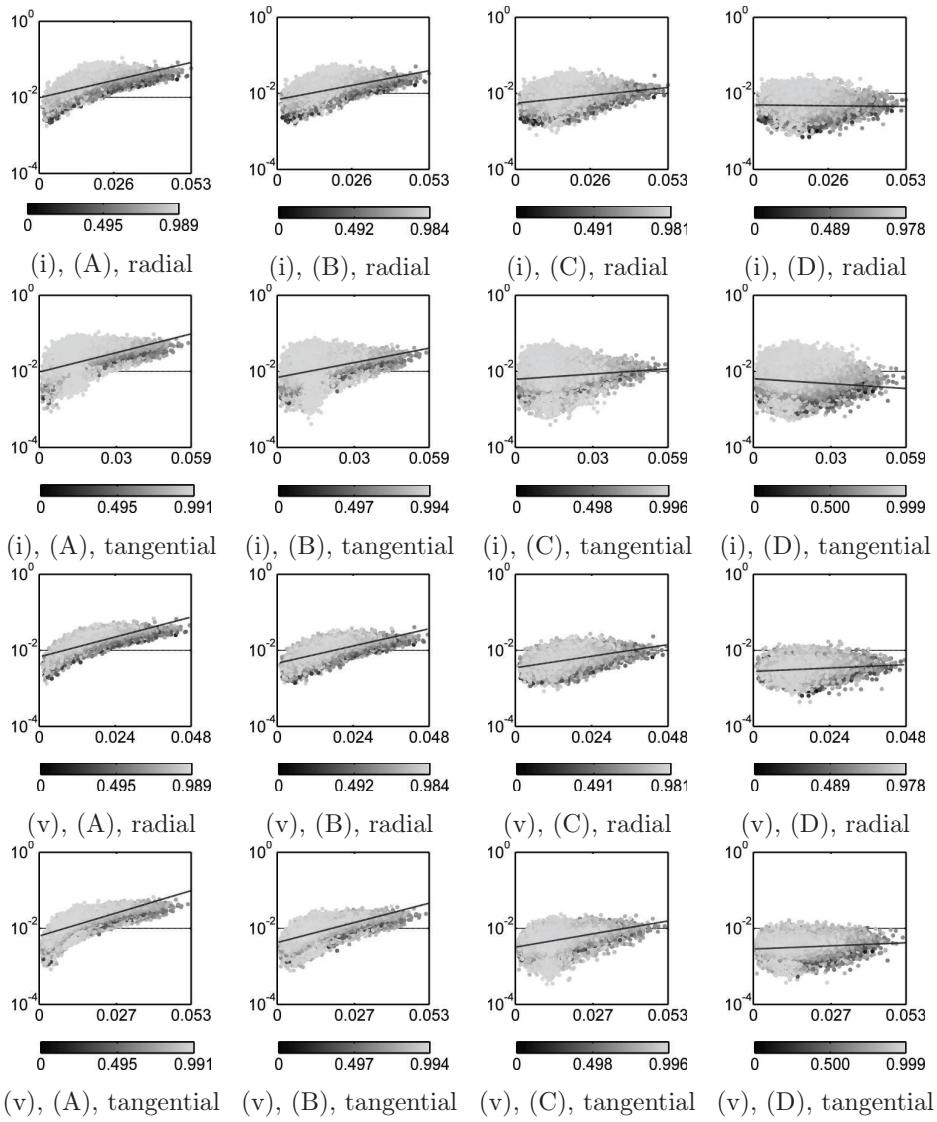

Figure 5. The relative error RE_k in the forward simulation tests (i) and (v) plotted against the distance (9) and visualized on a logarithmic scale separately for basically radially and tangentially directed sources, as well as for the dipole location candidates (A)–(D). The line showing the tendency corresponds to the least squares fit on a logarithmic scale and the color of each point shows the eccentricity of the corresponding dipole.

number of the Raviart-Thomas basis functions in the case of FEM (table 3), whereas in the BEM forward simulation, it was constantly 21624.

3.1. FEM forward simulation

The forward simulation tests performed are reported in table 5. The tests (i)–(viii) concerned the FEM with different dipole candidate locations, mesh resolutions and head models. The accuracy of $\mathbf{L}$ was measured in terms of the column- and matrix-wise

Table 8. The maximum of the angular error AE_k (degrees) in the forward simulation tests (i)–(viii) with the dipole locations (A)–(D).

	Dipole location			
Test	(A)	(B)	(C)	(D)
(i)	1.85	0.00000191	0.00000191	0
(ii)	7.56	4.70	1.90	2.62
(iii)	6.60	6.60	6.16	6.41
(iv)	8.10	4.88	3.38	12.85
(v)	1.85	0.00000191	0.00000191	0
(vi)	4.71	2.23	0.00000191	0
(vii)	5.91	3.03	0.0808	0.000349
(viii)	6.06	2.72	0.00000171	0

Table 9. The maximal eccentrity of basically radially and tangentially oriented dipole sources with the different finite element mesh resolutions and dipole candidate locations.

			Dipole location			
Orientation	Test	Resolution	(A)	(B)	(C)	(D)
Radial	(i),(v)	1	0.989	0.984	0.981	0.978
Tangential	(i),(v)	1	0.991	0.994	0.996	0.999
Radial	(ii),(vi)	2	0.960	0.952	0.946	0.940
Tangential	(ii),(vi)	2	0.960	0.976	0.986	0.999
Radial	(iii),(vii)	3	0.982	0.978	0.975	0.973
Tangential	(iii),(vii)	3	0.985	0.990	0.994	0.999
Radial	(iv),(viii)	4	0.919	0.903	0.892	0.878
Tangential	(iv),(viii)	4	0.920	0.950	0.971	0.997

Table 10. The relative error RE_L in the forward simulation tests (ix)–(xii) with the different values of the maximal dipole eccentricity.

	Maximal dipole eccentricity			
Test	0.997	0.986	0.979	0.969
(ix)	0.253	0.0312	0.0115	0.00472
(x)	0.277	0.0624	0.0522	0.0484
(xi)	0.341	0.108	0.0867	0.0796
(xii)	0.492	0.170	0.120	0.0946

relative errors

$$\mathrm{RE}_k = \frac{\|\mathbf{l}_k - \mathbf{l}_k^{\mathrm{REF}}\|_2}{\|\mathbf{l}_k^{\mathrm{REF}}\|_2} \quad \text{and} \quad \mathrm{RE}_L = \sqrt{\frac{\sum_{k=1}^{M} \|\mathbf{l}_k - \mathbf{l}_k^{\mathrm{REF}}\|_2^2}{\sum_{k=1}^{M} \|\mathbf{l}_k^{\mathrm{REF}}\|_2^2}}, \tag{8}$$

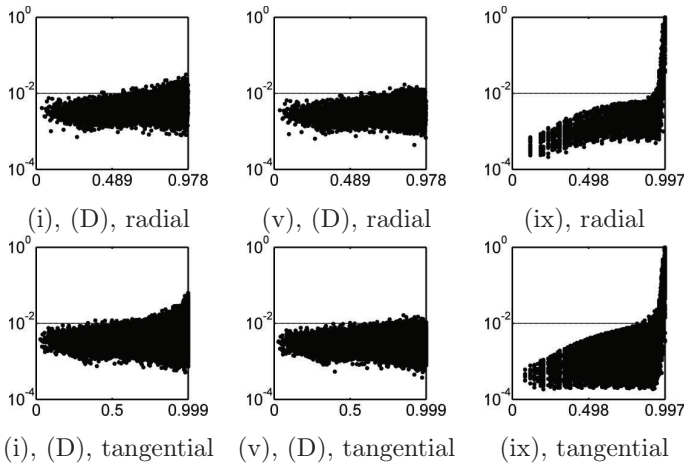

Figure 6. The relative error RE_k plotted against the dipole eccentricity in the FEM tests (i) and (v) with the dipole location (D) as well as in the BEM test (ix) with the maximal eccentricity of 0.997.

with $\mathbf{l}_k^{\mathrm{REF}}$ denoting the kth column of the reference matrix $\mathbf{L}^{\mathrm{REF}}$ computed through (7) with the same set of dipole moment and location pairs as in computation of $\mathbf{L}$. The column-wise RE_k was examined regarding its dependence on the distance

$$d_k = \|\mathbf{r}_k^{(D)} - \mathbf{r}_k^{(A)}\|_2 \tag{9}$$

as well as on the dipole eccentricity, i.e. on the distance from the domain center divided by the radius of the brain layer. The matrix-wise RE_L was used to measure the overall accuracy. In inverse dipole localization, the Raviart-Thomas source that best reproduces the dipole potential (7) was sought for each source location in the discretation. The accuracy of the fit was explored by finding the maximal localization and angular errors

$$\mathrm{LE}_k = \|\mathbf{r}_{j_k} - \mathbf{r}_k\|_2 \quad \text{and} \quad \mathrm{AE}_k = |\arccos(\mathbf{q}_{j_k} \cdot \mathbf{q}_k)|, \tag{10}$$

in which $j_k = \arg\min_j \|\mathbf{l}_j - \mathbf{l}_k^{\mathrm{REF}}\|_2$ is the index corresponding to the maximum likelihood [15]. Additionally, the maximal source eccentricity corresponding to the candidate locations (A)–(D) was computed.

3.1.1. Results The results are reported in tables 6–9 and figure 5. Table 6 shows that the dipole location (D) gives the best results of the candidates (A)–(D) in terms of the relative error RE_L. The largest relative error values were obtained with (A), for which RE_L was approximately from two to tree times as large as for (D). Figure 5 shows that with (A), (B) or (C) as the dipole location, RE_k plotted against the distance (9) has an increasing tendency, which is indicated by the slope of the least squares regression line. Moreover, the slope decreases when the dipole location is moved from (A) towards (D).

Regarding the inverse dipole fitting experiments, tables 7 and 8 document the maximum of the localization and angular error LE_k and AE_k together with the percentage of correctly localized dipoles, for which both errors are zero. According to these, the percentage of correctly localized dipoles was the highest, at least 99.98 %,

with the location (D) in each test. Additionally, the lowest value for the maximum of LE_k and AE_k was obtained with (D) in most of the tests.

The maximal source eccentricity corresponding to the candidate locations (A)–(D) is documented for both basically radially and tangentially oriented sources in table 9 showing that the highest source eccentricity applied in each of the tests (i)–(viii) was 0.997 or higher. In general, moving the dipole location from (A) towards (D) reduced the maximal eccentricity of the basically radial sources and increased the one of the basically tangential sources, respectively.

3.2. BEM forward simulation

The BEM forward simulation was used in the tests (ix)–(xii) (table 5), which were performed using the head model (I), authentic dipole sources, and different maximum limits for the eccentricity. The maximal eccentricities were 0.997, 0.986, 0.979, and 0.969. The relative errors RE_k and RE_L were computed, and the dependence RE_k on the eccentricity was studied. The results obtained through BEM were compared to the FEM ones.

3.2.1. Results The results are documented in table 10 and figure 6. Table 10 shows that in the case of the BEM forward simulation, the relative RE_L error grows rapidly when the maximal dipole eccentricity is increased. With the maximal eccentricity of 0.997 the values are very large and with 0.969 relatively small when compared to the values in table 6 obtained in the case of FEM. The further comparison between FEM and BEM displayed in figure 6 reveals that RE_k corresponding to BEM peaks near the surface of the brain layer and is again relatively small close to the domain center.

3.3. Numerical implementation and computation times

A PC equipped with a 2.2GHz dual-core processor and 4GB of RAM was used to compute the numerical experiments. The FEM forward simulation was tested both in a 32-bit and a 64-bit operating system and software environment. The BEM tests were carried out only in the former case. Implementation of the FEM was done through the MATLAB environment [10] using the method of preconditioned conjugate gradients (PCG) with the incomplete Cholesky preconditioner [5, 11] to produce the lead field matrix (4) as described in section 2.2. The residual norm value 10^{-6} was used as the PCG stopping criterion (tolerance). The applied MATLAB versions were 7.0 32-bit and 7.10 64-bit. And the MNE software's [14] implementation of the BEM was used to obtain the BEM lead field matrix.

3.3.1. Results The computation times have been included in table 5. Examination of the 32-bit results reveals that FEM provided the shorter computation time on all resolution levels. The difference is the most obvious when the number of elements is large; On the two finest resolution levels 1 and 2, the FEM required less than one sixth

and one third of the time taken by the BEM, respectively. Furthermore, MATLAB 7.10, 64-bit computed each FEM lead field matrix in less than one half of the time spent by MATLAB 7.0 32-bit.

4. Discussion

This study concerned the finite element method (FEM) applied to EEG from both forward and inverse aspects. A dipole source model based on lowest-order Raviart-Thomas basis functions [5, 21] was both defined and numerically evaluated. Each lowest order Raviart-Thomas basis function $\mathbf{w}_k$ was associated with a dipole $(\mathbf{q}_k, \mathbf{r}_k)$ defining the dipole moment as the volume integral of $\mathbf{w}_k$ and the location as a weighted average position of the vertices corresponding to $\mathbf{w}_k$. Four *ad hoc* candidates (A)–(D) (table 2) were tested as the location. Two spherical multi-layer head models were used: an isotropic three-layer (I) [1, 34] and an anisotropic four-layer model (II) [29, 8]. Both models were examined using four different mesh resolutions. The forward simulation accuracy was studied through the relative errors RE_k and RE_L (8), and the accuracy in inverse dipole localization was examined by finding the maxima of the localization and angular errors LE_k and AE_k (10). The reference forward simulation was obtained through the closed-form approach (7) [34].

The choice for the source location was found to be critical for the accuracy of the FEM forward simulation. The results concerning the tests (i)–(viii) suggest that (D) as the dipole location leads to the most accurate results in terms of RE_L. The largest error values were obtained with (A), for which RE_L was approximately from two to tree times as large as for (D). Moreover, the distance between (A) and (D) seems to have the smallest effect on RE_k, when the dipole location is the latter one.

The inverse dipole localization results also support the superiority of (D), as the maxima of LE_k and AE_k were in general lower with it than with the other candidates. With (D), the percentage of correctly localized dipoles ($\mathrm{LE}_k = \mathrm{AE}_k = 0$) was over 99.98 % in each test (i)–(viii) showing that accuracy provided by the lowest order Raviart-Thomas sources is sufficient regarding the EEG inverse problem. The maximum likelihood approach used in this study is extensively utilized for solving inverse problems in many different applications [15].

The definition (6) of the dipole moment can be seen as a rather straightforward one; an integrated current density is associated with a point current. Based on the numerical results, it seems to provide a robust simulation of the dipole direction and strength. It also seems that defining the dipole location as some integral of the basis function would not lead to as accurate results as (D). Namely, the three other candidate locations can be seen to better represent an integrated location, as they give more weight to the vertices, in which the basis function differs from zero (figure 3).

Despite the encouraging results obtained with (D), it is vital to stress that (D) is not claimed to be optimal as a source location. For example in test (iv), the best accuracy corresponds to (C) instead of (D). Finding the generally optimal location

would, however, obviously be very difficult because the location is to be determined by a single Raviart-Thomas element and, at the same time, the surrounding finite element mesh can, in principle, be arbitrary.

In addition to FEM, the BEM provided by the MNE software package [14] was used in forward simulation. The relative error RE_L for BEM was found to be strongly dependent on the maximal dipole eccentricity as compared to the case of FEM. The maximal eccentricity of 0.997 resulted in all of the BEM tests (ix)–(xii) into a larger RE_L than in any of the FEM tests (i)–(viii) (tables 6 and 9). Furthermore, RE_k plotted against the dipole eccentricity shows, that of the present FEM and BEM forward simulations, the latter one can be considerably less accurate near the surface of the brain layer and again more precise close to the domain center.

The results regarding the computation times suggest that FEM is, within the present experimental arrangement, substantially faster than BEM. This supports the computational effectiveness of the present approach and is also in good agreement with what is generally known about BEM and FEM; The BEM system matrix has only few zero matrix entries, and therefore, the time required for solving a linear system increases very rapidly as the system size grows. The FEM system matrix, in contrast, has a large number of zeros, which enables fast approximative solution through iterative methods.

The reduced accuracy of BEM with extremely eccentric sources is obviously caused by the singularity of the BEM integrals [3, 23], which leads the error in numerical integration to increase rapidly, when the dipole is brought into the vicinity of a surface mesh. Due to the singularity, the performance of BEM can be enhanced using high-order quadratures [23]. However, it is important to point out that in the practical applications extremely eccentric sources can typically be excluded as irrelevant: e.g. according to [1], most sources can be expected to be located between the eccentricities 0.6 and 0.9.

In the present FEM approach, the integrals that need to be computed are of the form (3) and (6). In the tetrahedral part of the mesh, a first order quadrature provides exact integration because the basis functions are all linear. In the prismatic part, a product formula combining triangular and one-dimensional first order quadratures can be used to provide exact integration results [26]. Consequently, high order quadratures are not needed in the implementation making it easily accessible. This contrasts to BEM and also to some FEM based forward simulations, e.g. the recent subtraction approach [18, 8], in which increasing the quadrature order improves the performance, because the source function for FEM is not polynomial.

Moreover, the present forward simulation appears to be also very accurate as compared to the subtraction approach, which is studied in [18, 8] via the same head model (II) as used in this study. The test (v) corresponding to the head model (II), and the mesh of 231 749 elements yielded the matrix-wise relative error RE_L equals 0.00327 with location (D) (table 6). Again, in the most accurate case presented in [8], the number of elements is 2 165 281, and the column-wise relative error varies between 0.002–0.006 ([8], Fig. 5 on page 1062) suggesting that the corresponding matrix-wise RE_L would satisfy $0.002 \leq \mathrm{RE}_L \leq 0.006$, since always $\min_k \mathrm{RE}_k \leq \mathrm{RE}_L \leq \max_k \mathrm{RE}_k$. In the case

of 1 712 360 elements ([8], Fig. 5 on page 1062), a similar argument results into estimate $0.008 \leq \mathrm{RE}_L \leq 0.017$. Hence, it appears that the approach presented in this study can achieve a given level of accuracy with fewer elements than what is required by the subtraction approach. Fewer elements would again probably mean shorter computation times, since matrices needed in computation of the lead field matrix would be smaller.

Finally, based on the encouraging results of this study, an interesting topic for the future work would be, for example, to directly compare, within a single study, the performance of the present approach to other FEM based forward simulations, e.g. in the spirit of [18] in which the subtraction approach is compared to Saint-Venant and partial integration approaches. Other interesting topics for future studies with Raviart-Thomas sources would be extended sources, e.g. multipoles [20] and dipole clusters, as well as the applications of [6, 7, 27].

5. Conclusions

This study concerned the finite element method (FEM) applied to EEG. A source model, in which a lowest-order Raviart-Thomas basis function was associated with a dipole moment and location, was both defined and numerically evaluated. Four *ad hoc* candidates were tested as the dipole location. Regarding the EEG inverse problem, the results of the numerical experiments verified a clear correspondence to the actual dipoles from both forward and inverse apects. As for the forward part, the matrix-wise relative errors as small as 0.00948 and 0.00372 were obtained for the two tested head models. And as for the inverse part, 99.98 % of the lowest-order Raviart-Thomas sources were correctly positioned in each dipole localization experiment with location (D). The accuracy of FEM was found to be substantially better for extremely eccentric sources than that of BEM due to errors related to numerical computation of the singular BEM integrals. Thus, the present FEM approach is advantageous as the integrals are low order polynomials and exact numerical integration is feasible with simple quadratures. Based on the numerical results it also seems that the accuracy of the present approach is comparable or even superior to the FEM based subtraction approach. Moreover, the present approach seems to be advantageous also regarding the computation time. An interesting topic for the future work would be to directly compare the performance of the present approach to other FEM forward simulation schemes, to study extended sources instead of dipoles, as well as to use the Raviart-Thomas sources in EEG applications.

Acknowledgments

SP's work was supported financially by Academy of Finland, yr. 2009, no. 136412.

Appendix. Entries of the matrix G

This appendix shows that the matrix $\mathbf{G}$ given by $g_{ik} = -\int_\Omega (\nabla \cdot \mathbf{w}_k)\, dV$ has exactly two nonzero entries in each column, when $\mathbf{w}_k$ is a lowest order Raviart-Thomas basis function and ψ_i is a linear nodal basis function. It is assumed that the vertices associated with $\mathbf{w}_k$ are numbered as in figure 2. The tetrahedron pair (1,2,3,4) and (1,2,3,5) in figure 2 is denoted by T_1 and T_2 and the face (1,2,3) by F.

The restriction of $\mathbf{w}_k$ to each tetrahedron is of the form (5), meaning that the normal component of $\mathbf{w}_k$ is nonzero only on F of all the faces and that the Gauss' divergence theorem can be written as $\Phi_k = \int_F \mathbf{w}_k \cdot \mathbf{n}\, dS = (-1)^\ell \int_{T_\ell} \nabla \cdot \mathbf{w}_k \, \mathrm{d}V$ for $\ell = 1, 2$. The piecewise linearity of $\mathbf{w}_k$ implies that $\nabla \cdot \mathbf{w}_k$ is constant on each tetrahedron, which combined with the divergence theorem gives $\nabla \cdot \mathbf{w}_k|_{T_\ell} = (-1)^\ell \Phi_k / V_\ell$ with $\ell = 1, 2$ and V_ℓ denoting the volume of the T_ℓ.

If ψ is a general linear nodal basis function supported on tetrahedron T, if A is the area of the face on which ψ vanishes and h is the corresponding tetrahedron height, the volume of T is given by $V = Ah/3$ and $\int_T \psi \, dV = \int_0^h Az^3/h^3 \, dz = Ah/4 = 3V/4$. Consequently, denoting by $\psi_1, \psi_2, \ldots, \psi_5$ the linear nodal basis functions associated with the vertices $1, 2, \ldots, 5$, respectively, the matrix entries $g_{ik} = -\int_\Omega (\nabla \cdot \mathbf{w}_k)\psi_i \, dV = -(\nabla \cdot \mathbf{w}_k) \int_\Omega \psi_i \, dV$ satisfy $g_{ik} = (3/4)\Phi_k V_1/V_1 - (3/4)\Phi_k V_2/V_2 = 0$, for $i = 1, 2, 3$, and $g_{4k} = -g_{5k} = (3/4)\Phi_k$. Hence, the only nonzero entries in kth column are g_{4k} and g_{5k}.

References

[1] Ary J P, Klein S A and Fender D H 1981 Location of sources of evoked scalp potentials: corrections for skull and scalp thicknesses *IEEE Trans. Biomed. Eng.* **28** 447–52

[2] Ataseven Y, Akalin-Acar Z, Acar C E, and Gencer N G 2008 Parallel implementation of the accelerated BEM approach for EMSI of the human brain *Med. Biol. Eng. Comput.* **46**(7) 671–679

[3] Beer G, Smith I and Duenser C 2008 *The Boundary Element Method with Programming: For Engineers and Scientists* (Berlin: Springer)

[4] Berg P and Scherg M 1994 A fast method for forward computation of multiple-shell spherical head models *Electroenceph. Clin. Neurophysiol.* **90** 58–64

[5] Braess D 2001 *Finite Elements* (Cambridge: Cambridge University Press)

[6] Calvetti D, Hakula H, Pursiainen S and Somersalo E 2009 Conditionally Gaussian Hypermodels for Cerebral Source Localization *SIAM J. Imaging Sci.* **2** 879–909

[7] Campi C, Pascarella A, Sorrentino A and Piana M 2008 A Rao-Blackwellized particle filter for magnetoencephalography *Inverse Problems* **24** 025023

[8] Drechsler F, Wolters C H, Dierkes T, Si H and Grasedyck L 2009 A full subtraction approach for finite element method based source analysis using constrained Delaunay tetrahedralisation *NeuroImage* **46** 1055–1065

[9] Ermer J, Mosher J C, Baillet S and Leahy R M 2001 Rapidly recomputable EEG forward models for realistic head shapes *Phys. Med. Biol.* **46** 1265–1281

[10] Ferreira A J M 2009 *MATLAB Codes for Finite Element Analysis* (Berlin: Springer)

[11] Golub G and van Loan C 1989 *Matrix Computations* (Baltimore: The John Hopkins University Press)

[12] Hämäläinen M and Ilmoniemi R 1994 Interpreting magnetic fields of the brain: minimum norm estimates *Med. & Biol. Eng. & Comput.* **32** 35–42

[13] Hämäläinen M, Hari R, Ilmoniemi R J, Knuutila J and Lounasmaa O V 1993 Magnetoencephalography — theory, instrumentation, and applications to invasive studies of the working human brain *Reviews of Modern Physics* / **65** 413–498

[14] Hämäläinen M 2009 MNE software user's guide version 2.7 `http://www.martinos.org/meg/manuals/MNE-manual-2.7.pdf`

[15] Kaipio J P and Somersalo E 2004 *Statistical and Computational Methods for Inverse Problems* (Berlin: Springer)

[16] Kybic J, Clerc M, Faugeras O, Keriven R and Papadopoulo T 2006 Generalized Head Models for MEG/EEG: Boundary Element Method Beyond Nested Volumes *Phys. Med. Biol.* **51**(5) 1333–1346

[17] Lew S, Wolters C H, Anwander A, Makeig S and MacLeod R S 2009 Improved EEG source analysis using low-resolution conductivity estimation in a four-compartment finite element head model *Human brain mapping* **30**

[18] Lew S, Wolters C H, Dierkes T, Röer C and MacLeod R S 2009 Accuracy and run-time comparison for differential potential approaches and iterative solvers in finite element method based EEG source analysis *Applied Numerical Mathematics* **59** 1970–1988

[19] Mosher J, Lewis P and Leahy R 1992 Multiple dipole modeling and localization from spatio-temporal MEG data *IEEE Trans. Biomed. Eng.* **39** 541–557

[20] Mosher J C, Leahy R M and Lewis P S 1999 EEG/MEG: Forward Solutions for Inverse Methods *IEEE Trans. Biomed. Eng.* **46** 245–259

[21] Monk P 2003 *Finite Element Methods for Maxwell's Equations* (Oxford, UK: Clarendon Press)

[22] Niedermeyer E and Lopes da Silva F 2004 *Electroencephalography: Basic Principles, Clinical Applications, and Related Fields Fifth Edition* (Philadelphia: Lippincott Williams & Wilkins)

[23] Ozgener B and Ozgener H A 2000 Gaussian quadratures for singular integrals in BEM with applications to the 2D modified Helmholtz equation *Eng. Anal. Bound. Elem.* **24** 259–269

[24] Pascual-Marqui R D, Michel C and Lehman D 1994 Low resolution electromagnetic tomography: A new method for localizing electrical activity in the brain *Int. J. Psycophysiol.* **18** 49–65

[25] Pascual-Marqui R D 1999 Review of Methods for Solving the EEG Inverse Problem *International Journal of Bioelectromagnetism* **1**(1) 75–86

[26] Solin P, Segeth K and Dolezel I 2003 *Higher-Order Finite Element Methods* (Boca Raton: Chapman & Hall / CRC)

[27] Sorrentino A, Parkkonen L, Pascarella A, Campi C and Piana M 2009 Dynamical MEG source modeling with multi-target Bayesian filtering *Human Brain Mapping* **30** 1911–1921

[28] Somersalo E, Voutilainen A and Kaipio J 2003 Non-stationary magnetoencephalography by Bayesian filtering of dipole models *Inverse Problems* **19** 1047–1063

[29] Stok C J 1987 The influence of model parameters on EEG/MEG single dipole source estimation *IEEE Trans. Biomed. Eng.* **34** 289–296

[30] Tanzer O, Järvenpää S, Nenonen J and Somersalo E 2005 Representation of bioelectric current sources using Whitney elements in the finite element method *Phys. Med. Biol.* **50** 3023–3039

[31] Uutela K, Hämäläinen M and Somersalo E 1999 Visualization of Magnetoencephalographic Data Using Minimum Current Estimates *NeuroImage* **10** 173–180

[32] Wolters C H, Anwander A, Tricoche X, Weinstein D, Koch M A and MacLeod R S 2006 Influence of tissue conductivity anisotropy on EEG/MEG field and return current computation in a realistic head model: a simulation and visualization study using high-resolution finite element modeling *NeuroImage* **30** 813–826

[33] Van Veen B D, Van Drongelen W, Yuchtman M and Suzuki A 1997 Localization of Brain Electrical Activity via Linearly Constrained Minimum Variance Spatial Filtering *IEEE Trans. Biomed. Eng.* **44** 867–880

[34] Zhang Z 1995 A fast method to compute surface potentials generated by dipoles within multilayer anisotropic spheres *Phys. Med. Biol.* **40** 335–349